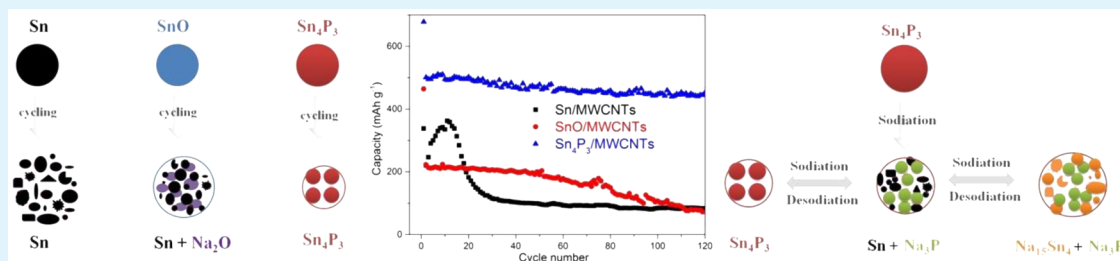


# Building Self-Healing Alloy Architecture for Stable Sodium-Ion Battery Anodes: A Case Study of Tin Anode Materials

Jianfeng Mao, Xiulin Fan, Chao Luo, and Chunsheng Wang\*

Department of Chemical and Biomolecular Engineering, University of Maryland, College Park, Maryland 20742, United States



**ABSTRACT:** The rational design of anode materials is a challenge in developing sodium ion batteries. Alloy anodes provide high gravimetric and volumetric capacities but suffer the short cycle life as a result of the continuous and accumulated pulverization, resulting from a large volume change during the cycling process. Herein, using pure Sn, an irreversible conversion reaction combined with an alloy reaction (SnO), and a reversible conversion reaction combined with an alloy reaction (Sn<sub>4</sub>P<sub>3</sub>) as samples, we demonstrate that the pulverization and aggregation of the alloy anode can be partially recovered and the accumulation of pulverization and aggregation during charge/discharge cycles can be terminated using a reversible conversion reaction combined with an alloy reaction. The cycling stability of three Sn-based anodes increases in order of Sn<sub>4</sub>P<sub>3</sub> > SnO > Sn. The enhancement in Sn<sub>4</sub>P<sub>3</sub> can be attributed to a reversible reaction of Sn<sub>4</sub>P<sub>3</sub> + 9Na ↔ 4Sn + 3Na<sub>3</sub>P, which repairs the cracks, damage, and aggregation of Sn particles that occurred in the alloy process of 4Sn + 15Na ↔ Na<sub>15</sub>Sn<sub>4</sub> during cycling and, hence, terminates the pulverization. The repair mechanism looks like the self-healing feature in nature, where the damage can be healed by itself. Therefore, the suggested mechanism can be called self-healing, while the repaired anode can be termed as the self-healing anode. The use of self-healing strategies to build an electrode architecture is new and highly desirable because it can increase the cycle life and provide a general approach toward stable electrode materials.

**KEYWORDS:** sodium-ion batteries, alloy anode, tin anode, self-healing, cycling stability

## INTRODUCTION

As a result of the low cost, abundance, and wide distribution of sodium resources, sodium-ion batteries (SIBs) have been attracting wide attention as a possible alternative to lithium-ion batteries (LIBs), especially for the application in large-scale energy storage.<sup>1–4</sup> More importantly, sodium has chemical properties similar to those of lithium, which makes it hopeful that the knowledge of lithium-ion technologies can be transformed to design SIB electrodes and, hence, enables the quick development of SIBs. However, challenges still remain because there are some fundamental differences between NIBs and LIBs.<sup>5</sup> For example, the ionic radius of Na<sup>+</sup> is larger than Li<sup>+</sup> (1.02 versus 0.76 Å). The larger Na<sup>+</sup> ions will lead to slower ion transport, more sluggish reaction kinetics, and larger volume change upon Na<sup>+</sup>/Na insertion/extraction, which usually results in limited rate capability and Na-storing reversibility.

Development of high capacity and long cycle life of anode materials is critical for the success of SIBs.<sup>6,7</sup> One of the widely studied anodes for NIBs is carbonaceous materials.<sup>8–21</sup> However, graphite, as the most commonly used anode material in LIBs, can only provide very small capacity in SIBs under normal conditions. A reasonable capacity was only obtained in

modified graphite via enlarging the interlayer distance or through co-intercalation with ether-based electrolytes.<sup>10–13</sup> The interest is also attracted on other carbon materials with low graphitization, where the Na storage is realized by combined Na intercalation and Na filling into the pores or defects.<sup>14–21</sup> For example, hard carbon has been found to have a sodiation capacity of 300 mAh/g, which is comparable to that of graphite in LIBs.<sup>14</sup> However, the volumetric capacity (450 mAh/cm<sup>3</sup>) is only about half of graphite in LIBs as a result of its low density (1.5 g/cm<sup>3</sup>).

Another type of the widely studied anodes for NIBs is alloy anodes.<sup>22</sup> A number of elements, such as Sn, Sb, Bi, Pb, and P, can form binary alloys with Na, such as Na<sub>15</sub>Sn<sub>4</sub> (847 mAh/g), Na<sub>3</sub>Sb (660 mAh/g), Na<sub>3</sub>Bi (385 mAh/g), Na<sub>15</sub>Pb<sub>4</sub> (485 mAh/g), and Na<sub>3</sub>P (2560 mAh/g), respectively.<sup>22–29</sup> Apparently, the Na–alloy anodes usually have higher gravimetric capacities than the carbonaceous anodes and could significantly improve the overall cell capacity. However, such an alloying reaction also has a large accompanied volume expansion. The associated volume

Received: January 18, 2016

Accepted: March 3, 2016

Published: March 3, 2016

expansion for forming  $\text{Na}_{15}\text{Sn}_4$ ,  $\text{Na}_3\text{Sb}$ ,  $\text{Na}_3\text{Bi}$ ,  $\text{Na}_{15}\text{Pb}_4$ , and  $\text{Na}_3\text{P}$  is 410, 290, 250, 365, and 490%, respectively. This enormous volume expansion will lead to a continuous and accumulated pulverization, resulting in fast capacity decay. Another issue for alloy anodes (i.e., Sn-based alloys) is the aggregation of the metal nanoparticles (i.e., Sn), further accelerating the pulverization and capacity decays.

To solve the issue of the pulverization and aggregation of the alloy particles during sodiation/desodiation cycling, a number of attempts have been developed to buffer the volume change of the alloy anodes during Na insertion and extraction reactions.<sup>30–38</sup> One method is to use an irreversible conversion reaction to *in situ* form an inactive matrix before the alloy reaction to alleviate the pulverization and aggregation of the alloy reaction.<sup>39,40</sup> For example, Sn oxides showed much longer cycling life than pure Sn because the inactive sodium oxide matrix formed during the initial irreversible conversion reaction ( $\text{SnO} + 2\text{Na} \rightarrow \text{Sn} + \text{Na}_2\text{O}$ ) can accommodate the volume change of formed nano-Sn and reduce the nano-Sn aggregation in the followed alloy reaction ( $4\text{Sn} + 15\text{Na} \leftrightarrow \text{Na}_{15}\text{Sn}_4$ ).<sup>40</sup> However, the irreversible conversion reaction reduces the first cycle Coulombic efficiency, and the sodium oxide matrix only alleviates the crack and aggregation of nano-Sn but does not recover the crack and prevent the aggregation of nano-Sn.

More recently, the  $\text{Sn}_4\text{P}_3/\text{C}$  anode experiencing conversion and alloy reactions has been found to exhibit a high capacity of 850 mAh/g, low first-cycle irreversible capacity of 250 mAh/g, and 86% capacity retention after 150 cycles.<sup>36–38</sup> The low irreversible capacity in the first charge/discharge cycle suggests that the conversion is highly reversible. Particularly, the cyclic stability of the  $\text{Sn}_4\text{P}_3/\text{C}$  composite anode is significantly enhanced in comparison to the individual Sn/C or P/C, and SnO anodes demonstrate that the reversible conversion reaction may be responsible for the long cycle life of  $\text{Sn}_4\text{P}_3/\text{C}$  anodes.<sup>36–38</sup> It seems that the pulverization and aggregation of Sn in the  $\text{Sn}_4\text{P}_3/\text{C}$  anode during the alloy reaction is partially repaired by the reversible conversion reaction during the sodiation/desodiation cyclings, and hence, the cyclability is promoted greatly.

To validate the recovery mechanism underlying the  $\text{Sn}_4\text{P}_3$  anode, a series Sn-based compounds, such as Sn/multi-walled carbon nanotubes (MWCNTs), SnO/MWCNTs, and  $\text{Sn}_4\text{P}_3/\text{MWCNTs}$  materials, have been prepared and compared as NIB anodes. Adding MWCNTs is to minimize the influence of electronic conductivity among these Sn-based anodes. We have shown that the electrochemical performance of  $\text{Sn}_4\text{P}_3/\text{MWCNTs}$  is superior to that of SnO/MWCNTs and Sn/MWCNTs. Furthermore, a self-healing mechanism is proposed, which provides a novel approach to modify the alloy anode and other electrodes with a large volume change during charging/discharging.

## EXPERIMENTAL SECTION

**Synthesis.** The raw chemicals Sn (97%) and SnO (97%) were purchased from Sigma-Aldrich;  $\text{Sn}_4\text{P}_3$  (99.5%) was obtained from Alfa-Aesar; and MWCNTs (10–30 nm in diameter and 1–2  $\mu\text{m}$  in length) were purchased from Nanostructured & Amorphous Materials, Inc. All of the materials are used as received. Sn, SnO, and  $\text{Sn}_4\text{P}_3$  were milled with the addition of 20 wt % MWCNTs at 400 rpm for 10 h using a Restch PM100 planetary.

**Material Characterization.** The crystal structure of the materials was characterized using powder X-ray diffraction (XRD) on a D8 Advanced with LynxEye and SolX (Bruker AXS, Madison, WI) using a Cu  $K\alpha$  radiation source. The morphology of the materials was

characterized using both Hitachi SU-70 analytical ultrahigh-resolution scanning electron microscopy (SEM) and JEOL 2100F LaB6 emission transmission electron microscopy (TEM) at the NanoCenter at the University of Maryland. The after-cycled electrode was rinsed with dimethyl carbonate (DMC) before taking the images.

**Electrochemical Measurements.** The electrodes were prepared by the slurry-coating method. The active materials (Sn/MWCNTs, SnO/MWCNTs, and  $\text{Sn}_4\text{P}_3/\text{MWCNTs}$ ) were mixed with carbon black and sodium alginate binder to form slurry at the weight ratio of 80:10:10. Then, the obtained slurry was cast on copper foil and dried in a vacuum oven at 100 °C overnight. The loading amount of active material was  $\sim 0.5 \text{ mg cm}^{-2}$ . Coin cells, consisting of a working electrode, a sodium metal counter electrode, Celgard 3501 separator, and 1.0 M  $\text{NaClO}_4$  in fluoroethylene carbonate/dimethyl carbonate (FEC/DMC, 1:1, v/v) co-solvent liquid electrolyte, were assembled in an argon-filled glovebox for electrochemical tests. Galvanostatic charge/discharge tests were performed on an Arbin battery test station (BT2000, Arbin Instruments, College Station, TX). The cells were cycled between 0.01 and 1.5 V under different current densities. All of the current densities used in this study were calculated on the basis of the Sn or Sn compound mass, such as Sn, SnO, or  $\text{Sn}_4\text{P}_3$ . Cyclic voltammetry (CV) testing under a scan rate of 0.1 mV/s was recorded using the Gamry Potentiostats (Gamry, Warminster, PA).

## RESULTS AND DISCUSSION

The Sn-based MWCNTs composites were prepared by ball milling. Figure 1 shows the XRD pattern of the as-milled Sn/

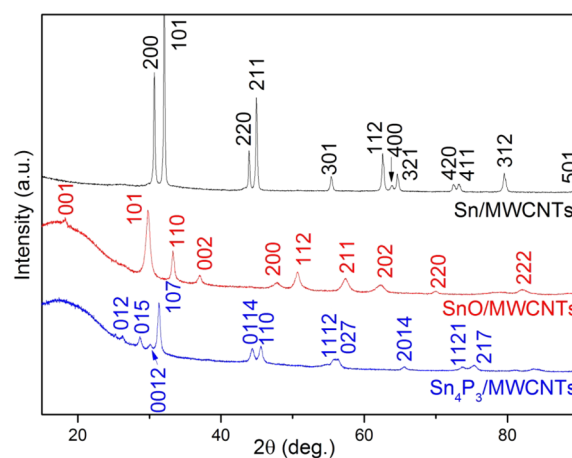


**Figure 1.** XRD patterns of Sn/MWCNTs, SnO/MWCNTs, and  $\text{Sn}_4\text{P}_3/\text{MWCNTs}$ .

MWCNTs, SnO/MWCNTs, and  $\text{Sn}_4\text{P}_3/\text{MWCNTs}$  materials. Clearly, the pattern shows pure Sn, SnO, and  $\text{Sn}_4\text{P}_3$  crystalline phases in the case of Sn/MWCNTs, SnO/MWCNTs, and  $\text{Sn}_4\text{P}_3/\text{MWCNTs}$ , respectively. The results show that the mechanical milling only produces a physical mixing. However, no peaks related to MWCNTs were observed, which is likely due to the low concentration as well as the formation of a nanocrystalline/disordered structure during the ball milling.

The morphology of the as-milled Sn/MWCNTs, SnO/MWCNTs,  $\text{Sn}_4\text{P}_3/\text{MWCNTs}$  was further investigated. Figure 2 shows the SEM image of the three samples. The particle sizes of the as-milled Sn/MWCNTs are around 10 nm (Figure 2a). In the case of SnO/MWCNTs, the morphology is irregular and consists of agglomerated particles from 100 nm to 2.5  $\mu\text{m}$  in size (Figure 2b). For the  $\text{Sn}_4\text{P}_3/\text{MWCNTs}$ , it also shows an irregular shape as well as microsized agglomerated  $\text{Sn}_4\text{P}_3$  particles, which are composed of primary nanoparticles from about 200 nm to 2.5  $\mu\text{m}$  in size (Figure 2c). The fact indicates

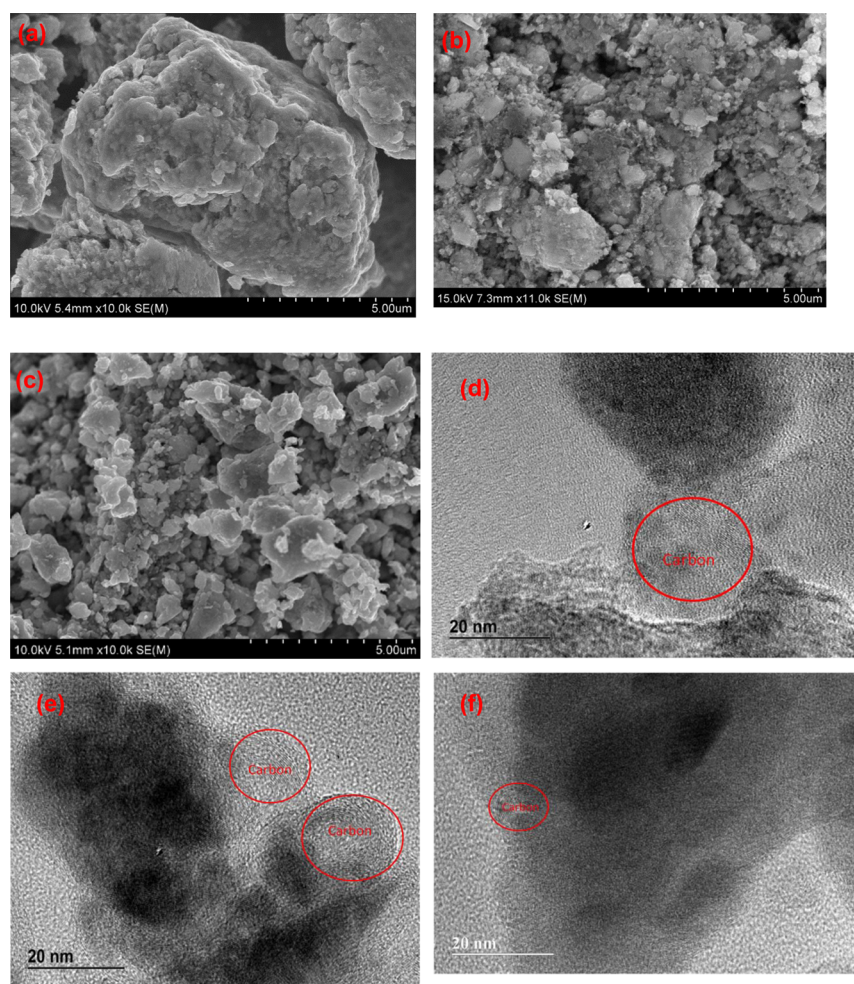


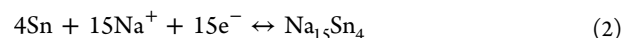
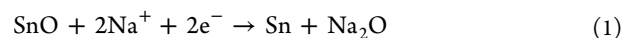
**Figure 2.** SEM images of (a) Sn/MWCNTs, (b) SnO/MWCNTs, and (c) Sn<sub>4</sub>P<sub>3</sub>/MWCNTs and HRTEM images for (d) Sn/MWCNTs, (e) SnO/MWCNTs, and (f) Sn<sub>4</sub>P<sub>3</sub>/MWCNTs.

that the presence of MWCNTs facilitates the ball mill efficiency and prevents the particle agglomeration. However, the MWCNTs are not observed clearly in these three samples, which is possible due to the fact that the MWCNTs may be damaged during ball milling. To identify the presence of MWCNTs, the high-resolution transmission electron microscope (HRTEM) images were taken for these three samples, as shown in panels d–f of Figure 2. Clearly, the lattice of MWCNTs can be observed and connected very well with the bulk materials. It further indicates that the MWCNTs were mixed very well during ball milling.

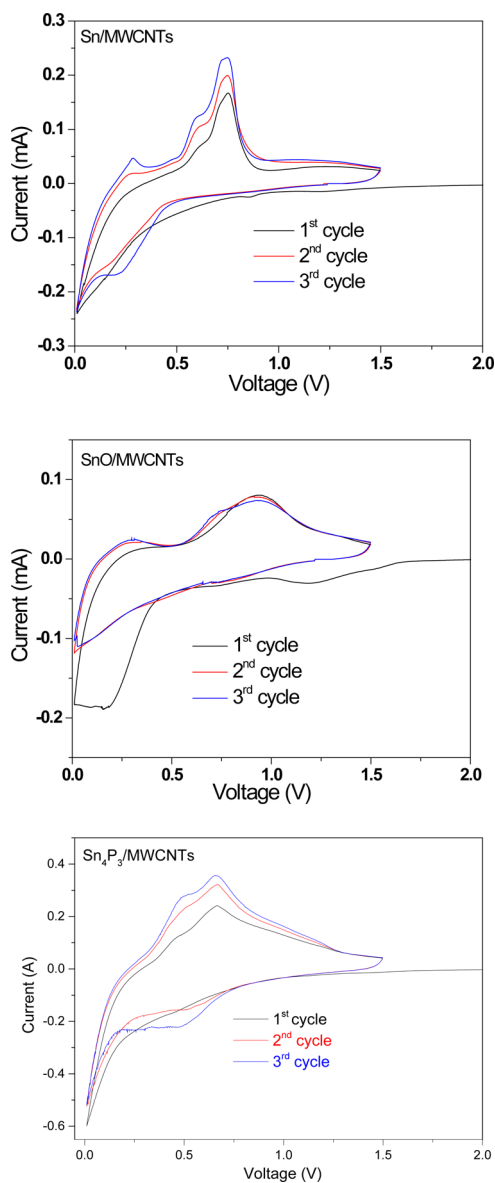
The electrochemical performance of the as-milled Sn/MWCNTs, SnO/MWCNTs, and Sn<sub>4</sub>P<sub>3</sub>/MWCNTs materials during sodiation/desodiation was investigated using coin cells in electrolytes of 1 M NaClO<sub>4</sub> in a mixture of FEC/DMC at 1:1 (v/v).

Figure 3 shows the cyclic voltammograms (CVs) of the as-milled Sn/MWCNTs, SnO/MWCNTs, and Sn<sub>4</sub>P<sub>3</sub>/MWCNTs materials in the first three cycles at a scan rate of 0.1 mV s<sup>-1</sup> between 0.01 and 1.5 V. For the Sn/MWCNTs, the large reduction peak from 0.8 to 0.01 V could be attributed the Na–Sn alloying reactions, with some contribution from the irreversible decomposition of the electrolyte. During sodiation, a series of Na–Sn alloys, such as NaSn<sub>5</sub>, NaSn, Na<sub>9</sub>Sn<sub>4</sub>, and Na<sub>15</sub>Sn<sub>4</sub>, will be generated. In the reversed anodic scans, several oxidative peaks with the most distinct peak at 0.7 V are

attributed to the dealloying reactions of Na–Sn compounds. For the SnO/MWCNTs, in the first cathodic scan, the peak at 1.16 V is associated with the irreversible decomposition of the electrolyte, while peaks ranging from 0.9 to 0.01 V are attributed to the irreversible conversion reaction of SnO with Na<sup>+</sup> to form Sn and Na<sub>2</sub>O (reaction 1) and the formation of Na<sub>x</sub>Sn alloys in the Na<sub>2</sub>O matrix (reaction 2). The large current difference between the first and following solidation is due to the irreversible conversion reaction of SnO (reaction 1).

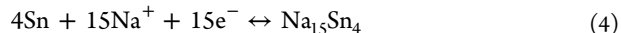
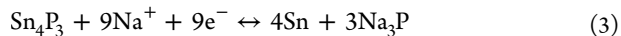


In the anodic scan, a broad oxidation peak around 0.9 V is attributed to desodiation from Na<sub>15</sub>Sn<sub>4</sub>. The more positive desodiation potential of SnO compared to Sn is due to the low conductivity of the Na<sub>2</sub>O matrix. In the case of Sn<sub>4</sub>P<sub>3</sub>/MWCNTs, a large reduction peak at 0.01 V and shoulder at 0.5 V are observed in the first cathodic scan and the shoulder current at 0.5 V increases to a peak in the following cathodic scans. In the first and subsequent anodic scans, two oxidative peaks at 0.46 and 0.65 V are observed, indicating two-step redox reactions. The CV results are in agreement with a previous report on Sn<sub>4</sub>P<sub>3</sub>-based materials<sup>35–37</sup> and further confirmed the two-step sodiation reactions of Sn<sub>4</sub>P<sub>3</sub>. During sodiation, Sn<sub>4</sub>P<sub>3</sub> first experiences a conversion reaction



**Figure 3.** CV curves of the first, second, and third cycles for the Sn/MWCNTs, SnO/MWCNTs, and Sn<sub>4</sub>P<sub>3</sub>/MWCNTs, respectively, at the scanning rate of 0.1 mV/s in the potential window of 0.01–1.5 V (versus Na<sup>+</sup>/Na).

(reaction 3) to form Sn and Na<sub>3</sub>P and then an alloy reaction (reaction 4) to form Na<sub>3</sub>P and Na<sub>15</sub>Sn<sub>4</sub>.



Although both SnO and Sn<sub>4</sub>P<sub>3</sub> experience the conversion reaction, the conversion reaction (reaction 1) of SnO is irreversible in the potential range between 0.01 and 1.5 V, while the conversion reaction (reaction 3) of Sn<sub>4</sub>P<sub>3</sub> is reversible.<sup>36</sup>

The charge/discharge profiles of the as-milled Sn/MWCNTs, SnO/MWCNTs, and Sn<sub>4</sub>P<sub>3</sub>/MWCNTs materials in the initial three cycles at a current of 100 mA/g are shown in Figure 4. The capacity is calculated on the basis of the total weight of Sn-based materials and MWCNTs. For Sn/MWCNTs, several discharge and charge plateaus are observed, which reflects the stepwise Na–Sn alloy phase transition

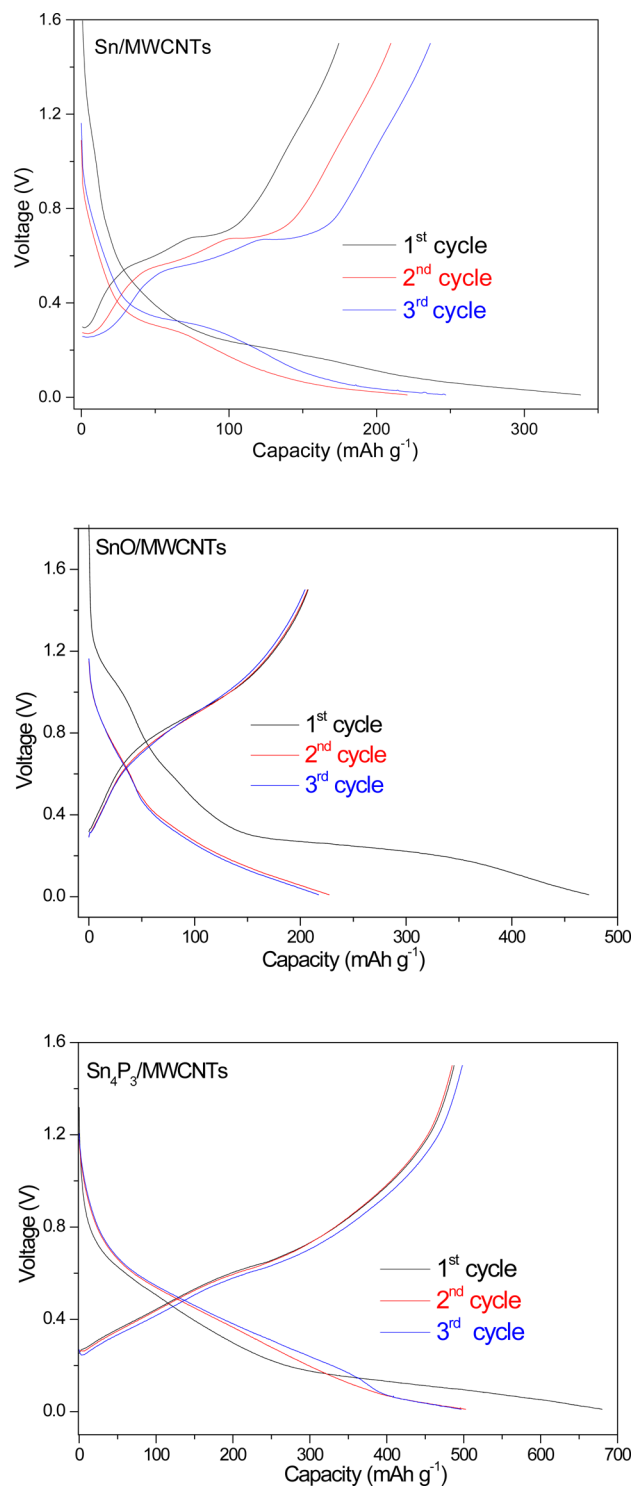


**Figure 4.** Galvanostatic charge/discharge curves of the first, second, and third cycles for the Sn/MWCNTs, SnO/MWCNTs, and Sn<sub>4</sub>P<sub>3</sub>/MWCNTs, respectively, at the current density of 100 mA/g within the potential window of 0.01–1.5 V (versus Na<sup>+</sup>/Na).

process. The first discharge capacity is 338 mAh/g, while the first charge only recovers a reversible capacity of 173 mAh/g. The delivered capacity increases in the following cycling, indicating that an activation process is required. Meanwhile, the initial Coulombic efficiency is only 51%. The low capacity is due to the pulverization and aggregation of Sn. For the SnO/MWCNTs, the first discharge curve displays the solid–

electrolyte interphase (SEI) formation feature at 1 V and the conversion reaction plateau at 0.25 V, which are agreeing well with the CV results. The first discharge capacity is 471 mAh/g, while the first charge only recovers a reversible capacity of 227 mAh/g. The initial Coulombic efficiency is only 48%, which is lower than Sn/MWCNTs as a result of the irreversible conversion reaction of SnO. However, the SnO/MWCNTs deliver stable capacities at the following cycles because the Na<sub>2</sub>O matrix reduces the aggregation of Sn and alleviates the stress/strain of Na<sub>x</sub>Sn. In the case of Sn<sub>4</sub>P<sub>3</sub>/MWCNTs, the charge/discharge profiles show two potential plateaus, corresponding to the conversion (reaction 3) and alloy (reaction 4) reactions, respectively. Meanwhile, the Sn<sub>4</sub>P<sub>3</sub> shows high discharge/charge capacities of 680/487 mAh/g. The initial Coulombic efficiency is 71.6%, which is higher than that of Sn/MWCNTs and SnO/MWCNTs materials.

The cyclic performance of the as-milled Sn/MWCNTs, SnO/MWCNTs, and Sn<sub>4</sub>P<sub>3</sub>/MWCNTs materials at 100 mA/g between 0.01 and 1.5 V versus Na<sup>+</sup>/Na is compared in Figure 5a. Among them, the Sn<sub>4</sub>P<sub>3</sub>/MWCNTs electrode exhibits the best cycling performance. The initial and second discharge capacities of the Sn<sub>4</sub>P<sub>3</sub>/MWCNTs electrode are 678 and 501 mAh/g, respectively. A total of 26% of irreversible capacity is ascribed to the formation of SEI, which consumes a certain percentage of sodium. After initial conditioning cycles, the capacity decay was very slow and a capacity of 452 mAh/g is maintained after 120 charge/discharge cycles, at only 0.086% decay per cycle compared to the second sodiation capacity. The Sn/MWCNTs electrode experiences an activation process in the first 10 cycles. The capacity is increased during the following cycles, and a capacity of 362 mAh/g is reached at the 11th cycle. However, after that, the capacity decays fast and only a capacity of 83 mAh/g is maintained after 120 discharge/charge cycles. For the SnO/MWCNTs electrode, the initial and second discharge capacities are 464 and 223 mAh/g, respectively. The capacity continuously decreases with charge/discharge cycles. Only a capacity of 72 mAh/g is left after 120 discharge/charge cycles. Obviously, the SnO/MWCNTs electrode is more stable than that of Sn/MWCNTs but worse than the Sn<sub>4</sub>P<sub>3</sub>/MWCNTs electrode. The Sn<sub>4</sub>P<sub>3</sub>/MWCNTs shows both the highest capacity and longest cycling stability in all three Sn-based compounds.

The cycling robustness of Sn<sub>4</sub>P<sub>3</sub>/MWCNTs is also tested at a lower current density because more Na ions will be inserted into Sn<sub>4</sub>P<sub>3</sub> at a low current; thus, the volume change of Sn<sub>4</sub>P<sub>3</sub>/MWCNTs in charge/discharge cycles becomes larger. Therefore, the capacity decay at a low current may become fast. Hence, the cycling performance of Sn<sub>4</sub>P<sub>3</sub>/MWCNTs under a low current density is also examined. Figure 5b shows the cycling performance of the Sn<sub>4</sub>P<sub>3</sub>/MWCNTs and SnO/MWCNTs electrodes at a low current density of 50 mA/g. SnO/MWCNTs electrodes at a low current show a faster capacity decay than that at a high current (Figure 5a), especially after 50 cycles, although the initial stable capacity (300 mAh/g) is higher than that (200 mAh/g) in a high current. In contrast, the cycling stability of Sn<sub>4</sub>P<sub>3</sub>/MWCNTs at a low current is even much better than that in a high current. The improved cycling stability of Sn<sub>4</sub>P<sub>3</sub>/MWCNTs at a low current can be attributed to enhanced self-healing effects as a result of a more complete reversible conversion reaction.

Not only the stable cycling performance but also the rate capability is very important for the electrodes toward practical applications. The Sn<sub>4</sub>P<sub>3</sub>/MWCNTs electrode also displayed

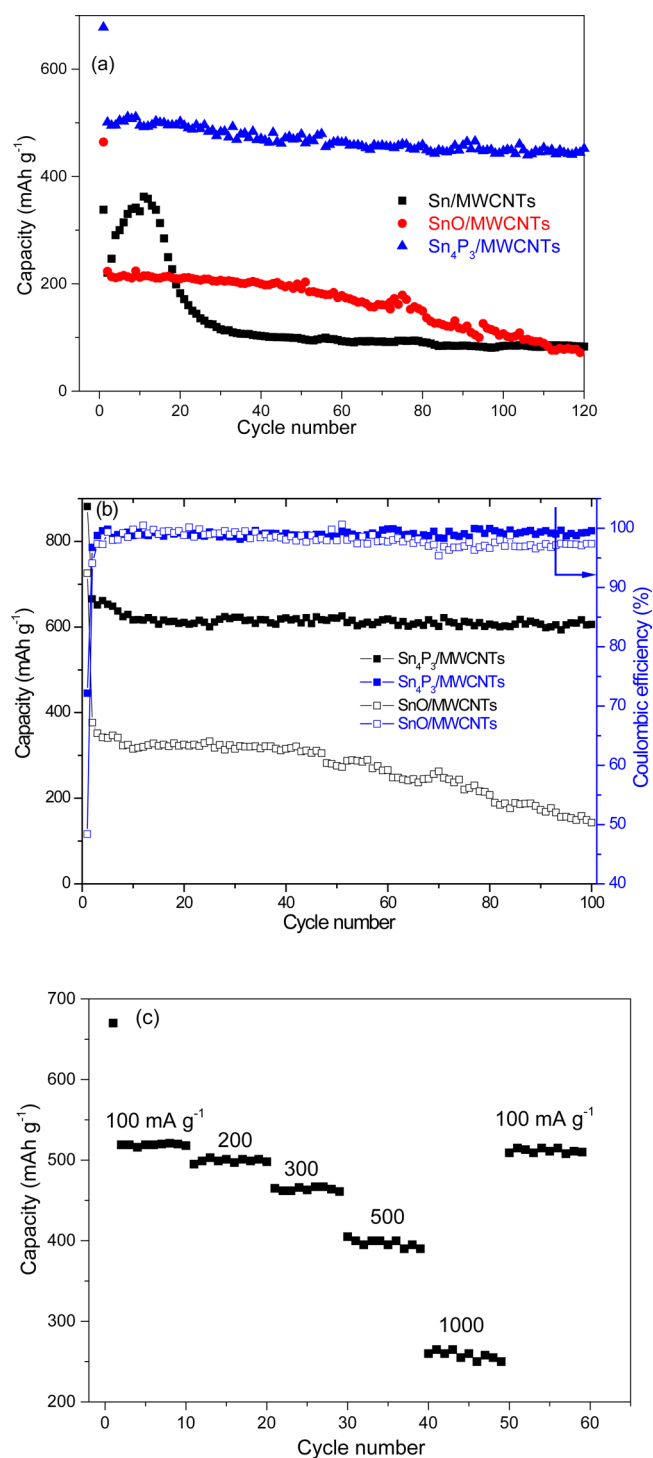


**Figure 5.** (a) Comparison of the cycling performances at 100 mA/g for the four samples of Sn/MWCNTs, SnO/MWCNTs, and Sn<sub>4</sub>P<sub>3</sub>/MWCNTs. (b) Comparison of the cycling performances at 50 mA/g for the SnO/MWCNTs and Sn<sub>4</sub>P<sub>3</sub>/MWCNTs. (c) Rate capabilities for the Sn<sub>4</sub>P<sub>3</sub>/MWCNTs at the varied current rates of 100–1000 mA/g.

excellent rate capability. As shown in Figure 4, the Sn<sub>4</sub>P<sub>3</sub>/MWCNTs electrode can deliver total reversible capacities of 520, 500, 464, 397, and 259 mAh/g at the current densities of 100, 200, 300, 500, and 1000 mA/g, respectively. Importantly, when the current density returns to 100 mA/g, the discharge capacity can recover to 512 mAh/g.

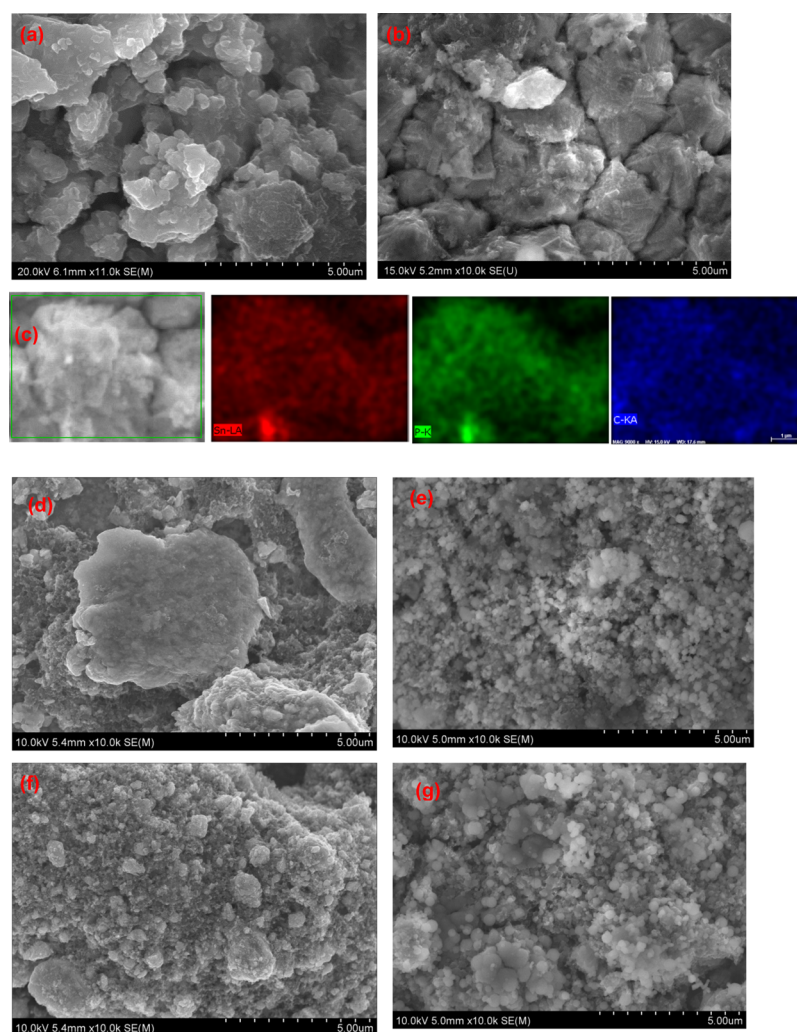


**Figure 6.** SEM images of the  $\text{Sn}_4\text{P}_3/\text{MWCNTs}$  electrode (a) before and (b) after 120 charge/discharge cycles at the current density of 100 mA/g. (c) EDS element mapping images of the  $\text{Sn}_4\text{P}_3/\text{MWCNTs}$  electrode after 120 charge/discharge cycles. SEM images of the  $\text{Sn}/\text{MWCNTs}$  electrode (d) before and (e) after 120 charge/discharge cycles at the current density of 100 mA/g. SEM images of the  $\text{SnO}/\text{MWCNTs}$  electrode (f) before and (g) after 120 charge/discharge cycles at the current density of 100 mA/g.

On the basis of the above results, it is clearly shown that the electrochemical performance of the  $\text{Sn}_4\text{P}_3/\text{MWCNTs}$  electrode is best among the investigated Sn-based electrodes. The possible reason is that the reversible conversion reaction healed the pulverization and crack induced by the alloy reaction. If so, the  $\text{Sn}_4\text{P}_3/\text{MWCNTs}$  electrode should maintain the original morphology. Therefore, the morphology after long-term cycling is examined by the post-cycling SEM and energy-dispersive X-ray (EDS) analysis. Figure 6 shows the SEM and EDS mapping images of the  $\text{Sn}_4\text{P}_3/\text{MWCNTs}$  after 120 charge/discharge cycles between 0.01 and 1.5 V at 100 mA/g. For comparison, the SEM image of a fresh  $\text{Sn}_4\text{P}_3/\text{MWCNTs}$  electrode was also included. Clearly, the morphology is well-maintained after the cycling test, suggesting the high structural stability and the architectural merit. This is further confirmed by the uniform distribution of Sn, P, and C in the  $\text{Sn}_4\text{P}_3/\text{MWCNTs}$  particles, as shown in the EDS mapping images. The results indicate that the volume expansion of Sn and P in the  $\text{Sn}_4\text{P}_3/\text{MWCNTs}$  electrode during charge/discharge could be partially self-healed (recovered). In contrast, for the case of  $\text{Sn}/\text{MWCNTs}$  (panels d and e of Figure 6) and  $\text{SnO}/\text{MWCNTs}$  (panels f and g of Figure 6), the morphology is changed after

cycling and the cracking and pulverization are observed in the electrodes. The continuous and accumulated pulverization could lead to the loss of electrical contact and excessive SEI growth and, hence, suffers from fast capacity decay and short cycle life, as shown in Figure 5.

The reversibility of the conversion reaction is critical for self-healing of the damage from the alloy process. The reversibility of the conversion reaction was examined by the phase changes upon sodiation/desodiation using *ex situ* XRD, as shown in Figure 7. Figure 7a shows the *ex situ* XRD of the  $\text{Sn}_4\text{P}_3/\text{MWCNTs}$  electrode upon discharge/charge. It can be seen that, upon sodiation to 0.6 V, the  $\text{Sn}_4\text{P}_3$  electrode shows a clear XRD pattern of the  $\text{Sn}_4\text{P}_3$  lattice. After sodiated to 0.01 V, the  $\text{Sn}_4\text{P}_3$  signals disappeared and the reflections of Sn,  $\text{Na}_{15}\text{Sn}_4$ , and  $\text{Na}_3\text{P}$  are observed. This observation agrees well with the previous report for the conversion and alloying reactions of  $\text{Sn}_4\text{P}_3$  to  $\text{Na}_3\text{P}$  and  $\text{Na}_{15}\text{Sn}_4$  upon sodiation.<sup>36–38</sup> The Sn signals still exist, indicating that part of Sn cannot accomplish the Na–alloy reaction at the end of the sodiation process. At reversed desodiation to 0.6 and 1.5 V, the XRD signals of the Sn,  $\text{Na}_{15}\text{Sn}_4$ , and  $\text{Na}_3\text{P}$  phases disappeared. It indicates that new materials should be regenerated, but no XRD peaks were

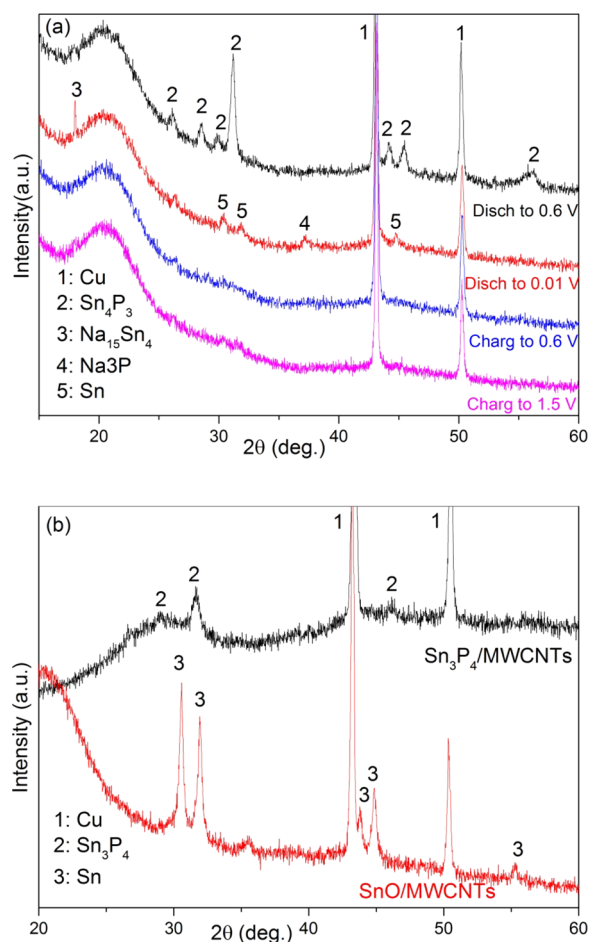


**Figure 7.** (a) *Ex situ* XRD patterns of the Sn<sub>4</sub>P<sub>3</sub>/MWCNTs electrode at different sodiation and desodiation states. (b) *Ex situ* XRD patterns of the Sn<sub>4</sub>P<sub>3</sub>/MWCNTs and SnO/MWCNTs electrodes after full desodiation at 1.5 V for 2 days.

detected. However, Kim et al. observed the XRD peaks of Sn<sub>4</sub>P<sub>3</sub> during desodiation at 1.5 V in their case.<sup>37</sup> In our case, this is presumably because the final reaction products may be too small to be detected by XRD. To increase the grain size of Sn<sub>4</sub>P<sub>3</sub>, we reduced the charging and discharging rate to 20 mA/g and kept it at 1.5 V for 2 days to allow for the Sn<sub>4</sub>P<sub>3</sub> phase to grow large enough to be easily detected by XRD. As shown in Figure 7b, several distinct peaks are detected in the Sn<sub>4</sub>P<sub>3</sub>/MWCNTs sample after full desodiation, which can be assigned to the Sn<sub>4</sub>P<sub>3</sub> phase. Therefore, it concludes that the sodiation/desodiation of Sn<sub>4</sub>P<sub>3</sub> via conversion and alloying reactions is reversible. For comparison, the full desodiation of the SnO/MWCNTs electrode at 1.5 V for 2 days is also investigated. As shown in Figure 7b, the reflection of Sn is clearly observed but no SnO phase is detected. It indicates that the conversion reaction of SnO is irreversible at 1.5 V. In contrast, the partially reversible formation of SnO upon sodiation/desodiation was only confirmed at 3 V.<sup>40</sup>

The self-healing mechanism of Sn<sub>4</sub>P<sub>3</sub> during sodiation/desodiation cycles is schematically shown in Figure 8. The morphology and structure changes of the Sn-based electrodes (Sn, SnO, and Sn<sub>4</sub>P<sub>3</sub>) before and after cycling are compared in Figure 8a as well as shown in Figure 6. For Sn anodes, the stress generated by the huge volumetric changes during the sodiation/desodiation of Sn causes pulverization, cracks, and aggregation in the Sn/MWCNTs electrode, resulting in the loss

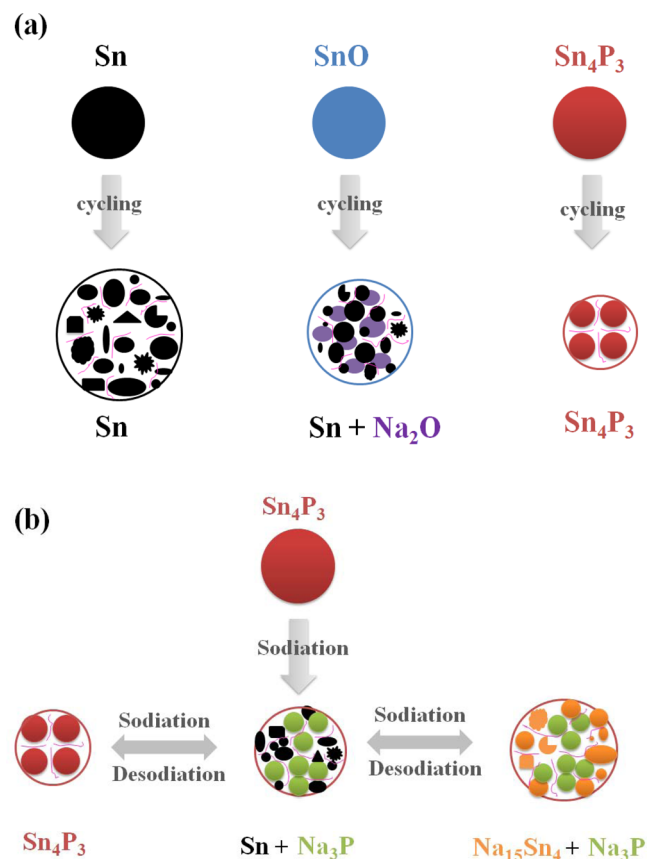


**Figure 8.** Schematic illustration for the (a) behavior of the Sn-based electrodes before and after cycling and (b) self-healing effect of the conversion reaction for the Sn<sub>4</sub>P<sub>3</sub> anode (with Sn in black, SnO in blue, Na<sub>4</sub>P<sub>3</sub> in red, Na<sub>3</sub>P in olive, Na<sub>15</sub>Sn<sub>4</sub> in orange, and cracks in pink).

of electrical contact and the subsequent loss of capacity, as evidenced by fast capacity decays with only a capacity of 83 mAh/g at 120 cycles (panels d and e of Figure 6). For SnO, the *in situ* formed small Sn particles (reaction 1) and Na<sub>2</sub>O matrix (reaction 2) reduce the cracking, help in preventing the aggregation of the Sn particles, and likely improve the overall mechanical stability of the electrode, leading to retarded cracking and crumbling during cycling, thus improving the cycling (panels f and g of Figure 6). In contrast, the conversion reaction of Sn<sub>4</sub>P<sub>3</sub> (reaction 3) in the Sn<sub>4</sub>P<sub>3</sub>/MWCNTs electrode is reversible (Figure 7b), and the Sn<sub>4</sub>P<sub>3</sub> structure is turned back after each cycling. Therefore, the pulverization of Sn of the Sn<sub>4</sub>P<sub>3</sub>/MWCNTs electrode is partially repaired by the reversible conversion reaction process during the sodiation/desodiation cycles (panels a–c of Figure 6). The self-healing effect of the reversible conversion reaction for alloying anodes is schematically illustrated in Figure 8b. For the Sn<sub>4</sub>P<sub>3</sub>/MWCNTs electrode, a conversion reaction undergoes first during sodiation, where the Sn<sub>4</sub>P<sub>3</sub> breaks into small Sn particles and Na<sub>3</sub>P matrix. Upon further sodiation, Na inserts into Sn to form Na<sub>15</sub>Sn<sub>4</sub> through the alloying reaction, which normally results in pulverization. During the desodiation, Na<sub>15</sub>Sn<sub>4</sub> dealloys first to form Sn and then Sn reacts with Na<sub>3</sub>P to convert back to Sn<sub>4</sub>P<sub>3</sub>. Thus, the cracks, damage, and aggregation of Sn induced in the (de)alloying process (reaction 4) is healed by this reversible conversion reaction (reaction 3).

Hence, the poor cycle stability of the alloy reaction is improved by the use of the reversible conversion reaction.

The positive effect of the reversible conversion reaction on the alloying anodes can be called self-healing. Because it is known that self-healing is widely present in biological systems, such as human skin, where the damage can be repaired by itself. Recently, the self-healing feature is also applied in rechargeable batteries to increase the cycle life. For example, Wang et al. reported that the poor cycle life of silicon anodes is overcome by coating a self-healing polymer, which repairs the cracks and damages spontaneously during cycling.<sup>41</sup> As a difference from Wang et al. using a self-healing polymer binder, we directly self-heal the active alloy. For the Sn/MWCNTs, only the alloy reaction takes place during cycling. However, in the Sn<sub>4</sub>P<sub>3</sub>/MWCNTs, two reversible reactions, including conversion and alloy reactions, happen during cycling. Also, the additional reversible conversion reaction may contribute to a higher capacity. The self-healing anode is new and highly desirable because it increases the cycle life and sheds light to develop alloy anodes for high-performance SIBs and rechargeable batteries.

## CONCLUSION

In summary, by investigating a series of Sn-based anodes (Sn/MWCNTs, SnO/MWCNTs, and Sn<sub>4</sub>P<sub>3</sub>/MWCNTs), a self-healing mechanism is highlighted in improving the performance of Na–alloy anodes. By introduction of a reversible conversion reaction, not only is the capacity increased but also the continuous pulverization of Sn in the alloy reaction during cycling is healed. Specifically, the most stable performance in the Sn<sub>4</sub>P<sub>3</sub>/MWCNTs among the investigated Sn anodes can be attributed to a reversible reaction of Sn<sub>4</sub>P<sub>3</sub> + 9Na ↔ 4Sn + 3Na<sub>3</sub>P, which repairs the cracks, damage, and aggregation of Sn in the alloy reaction during cycling. This new concept of self-healing can be easily extended to other alloy-type anode materials for overcoming the pulverization resulting from the large volume changes during cycling and may also be useful for other electrode materials that experience the same volume change issue.

## AUTHOR INFORMATION

### Corresponding Author

\*E-mail: cswang@umd.edu.

### Notes

The authors declare no competing financial interest.

## ACKNOWLEDGMENTS

Jianfeng Mao thanks the funding support from the United States Department of Energy (U.S. DOE)'s Advanced Research Projects Agency-Energy (ARPA-E) (DEAR0000389). Also, the authors acknowledge the support of the Maryland NanoCenter and its Advanced Imaging and Microscopy Laboratory (AIMLab).

## REFERENCES

- (1) Dunn, B.; Kamath, H.; Tarascon, J. M. Electrical Energy Storage for the Grid: A Battery of Choices. *Science* **2011**, *334*, 928–935.
- (2) Slater, M. D.; Kim, D.; Lee, E.; Johnson, C. S. Sodium-Ion Batteries. *Adv. Funct. Mater.* **2013**, *23*, 947–958.
- (3) Pan, H. L.; Hu, Y. S.; Chen, L. Q. Room-Temperature Stationary Sodium-Ion Batteries for Large-Scale Electric Energy Storage. *Energy Environ. Sci.* **2013**, *6*, 2338–2360.

- (4) Palomares, V.; Serras, P.; Villaluenga, I.; Hueso, K. B.; Carretero-Gonzalez, J.; Rojo, T. Na-Ion Batteries, Recent Advances and Present Challenges to Become Low Cost Energy Storage Systems. *Energy Environ. Sci.* **2012**, *5*, 5884–5901.

- (5) Yabuuchi, N.; Kubota, K.; Dahbi, M.; Komaba, S. Research Development on Sodium-Ion Batteries. *Chem. Rev.* **2014**, *114*, 11636–11682.

- (6) Chevrier, V. L.; Ceder, G. Challenges for Na-ion Negative Electrodes. *J. Electrochem. Soc.* **2011**, *158*, A1011–A1014.

- (7) Kim, Y. J.; Ha, K. H.; Oh, S. M.; Lee, K. T. High-Capacity Anode Materials for Sodium-Ion Batteries. *Chem. - Eur. J.* **2014**, *20*, 11980–11992.

- (8) Alcántara, R.; Jiménez-Mateos, J. M.; Lavela, P.; Tirado, J. L. Carbon Black: a Promising Electrode Material for Sodium-Ion Batteries. *Electrochem. Commun.* **2001**, *3*, 639–642.

- (9) Ge, P.; Foulletier, M. Electrochemical Interaction of Sodium in Graphite. *Solid State Ionics* **1988**, *28–30*, 1172–1175.

- (10) Jache, B.; Adelhelm, P. Use of Graphite as a Highly Reversible Electrode with Superior Cycle Life for Sodium-Ion Batteries by Making Use of Co-Intercalation Phenomena. *Angew. Chem., Int. Ed.* **2014**, *53*, 10169–10173.

- (11) Kim, H.; Hong, J.; Park, Y. U.; Kim, J.; Hwang, I.; Kang, K. Sodium Storage Behavior in Natural Graphite using Ether-based Electrolyte Systems. *Adv. Funct. Mater.* **2015**, *25*, 534–541.

- (12) Wang, Y. X.; Chou, S. L.; Liu, H. K.; Dou, S. X. Reduced Graphene Oxide with Superior Cycling Stability and Rate Capability for Sodium Storage. *Carbon* **2013**, *57*, 202–208.

- (13) Wen, Y.; He, K.; Zhu, Y.; Han, F.; Xu, Y.; Matsuda, I.; Ishii, Y.; Cumings, J.; Wang, C. Expanded Graphite as Superior Anode for Sodium-Ion Batteries. *Nat. Commun.* **2014**, *5*, 4033.

- (14) Stevens, D. A.; Dahn, J. R. The Mechanisms of Lithium and Sodium Insertion in Carbon Materials. *J. Electrochem. Soc.* **2001**, *148*, A803–A811.

- (15) Komaba, S.; Murata, W.; Ishikawa, T.; Yabuuchi, N.; Ozeki, T.; Nakayama, T.; Ogata, A.; Gotoh, K.; Fujiwara, K. Electrochemical Na Insertion and Solid Electrolyte Interphase for Hard-Carbon Electrodes and Application to Na-Ion Batteries. *Adv. Funct. Mater.* **2011**, *21*, 3859–3867.

- (16) Yan, Y.; Yin, Y.-X.; Guo, Y.-G.; Wan, L.-J. A Sandwich-Like Hierarchically Porous Carbon/Graphene Composite as a High-Performance Anode Material for Sodium-Ion Batteries. *Adv. Energy Mater.* **2014**, *4*, 1301584.

- (17) Wenzel, S.; Hara, T.; Janek, J.; Adelhelm, P. Room-Temperature Sodium-Ion Batteries: Improving the Rate Capability of Carbon Anode Materials by Templating Strategies. *Energy Environ. Sci.* **2011**, *4*, 3342–3345.

- (18) Cao, Y.; Xiao, L.; Sushko, M. L.; Wang, W.; Schwenzer, B.; Xiao, J.; Nie, Z.; Saraf, L. V.; Yang, Z.; Liu, J. Sodium Ion Insertion in Hollow Carbon Nanowires for Battery Applications. *Nano Lett.* **2012**, *12*, 3783–3787.

- (19) Tang, K.; Fu, L. J.; White, R. J.; Yu, L. H.; Titirici, M. M.; Antonietti, M.; Maier, J. Hollow Carbon Nanosphere with Superior Rate Capability for Sodium-Based Batteries. *Adv. Energy Mater.* **2012**, *2*, 873–877.

- (20) Chen, T. Q.; Liu, Y.; Pan, L. K.; Lu, T.; Yao, Y. F.; Sun, Z.; Chua, D. H. C.; Chen, Q. Electrospun Carbon Nanofibers as Anode Materials for Sodium Ion Batteries with Excellent Cycle Performance. *J. Mater. Chem. A* **2014**, *2*, 4117–4121.

- (21) Zhou, X. S.; Guo, Y. G. Highly Disordered Carbon as a Superior Anode Material for Room-Temperature Sodium-Ion Batteries. *ChemElectroChem* **2014**, *1*, 83–86.

- (22) Tran, T. T.; Obrovac, M. N. Alloy Negative Electrodes for High Energy Density Metal-Ion Cells. *J. Electrochem. Soc.* **2011**, *158*, A1411–A1416.

- (23) Ellis, L. D.; Wilkes, B. N.; Hatchard, T. D.; Obrovac, M. N. In Situ XRD Study of Silicon, Lead and Bismuth Negative Electrodes in Nonaqueous Sodium Cells. *J. Electrochem. Soc.* **2014**, *161*, A416–A421.

(24) Qian, J.; Wu, X.; Cao, Y.; Ai, X.; Yang, H. High Capacity and Rate Capability of Amorphous Phosphorus for Sodium Ion Batteries. *Angew. Chem., Int. Ed.* **2013**, *52*, 4633–4636.

(25) Kim, Y.; Park, Y.; Choi, A.; Choi, N.-S.; Kim, J.; Lee, J.; Ryu, J. H.; Oh, S. M.; Lee, K. T. An Amorphous Red Phosphorus/Carbon Composite as a Promising Anode Material for Sodium Ion Batteries. *Adv. Mater.* **2013**, *25*, 3045–3049.

(26) Ellis, L. D.; Hatchard, T. D.; Obrovac, M. N. Reversible Insertion of Sodium in Tin. *J. Electrochem. Soc.* **2012**, *159*, A1801–A1805.

(27) Datta, M. K.; Epur, R.; Saha, P.; Kadakia, K.; Park, S. K.; Kumta, P. N. Tin and Graphite Based Nanocomposites: Potential Anode for Sodium Ion Batteries. *J. Power Sources* **2013**, *225*, 316–322.

(28) Darwiche, A.; Marino, C.; Sougrati, M. T.; Fraisse, B.; Stievano, L.; Monconduit, L. Better Cycling Performances of Bulk Sb in Na-Ion Batteries Compared to Li-Ion Systems: An Unexpected Electrochemical Mechanism. *J. Am. Chem. Soc.* **2012**, *134*, 20805–20811.

(29) Zhu, Y. J.; Han, X. G.; Xu, Y. H.; Liu, Y. H.; Zheng, S. Y.; Xu, K.; Hu, L. B.; Wang, C. S. Electrospun Sb/C Fibers for a Stable and Fast Sodium-Ion Battery Anode. *ACS Nano* **2013**, *7*, 6378–6386.

(30) Xu, Y. H.; Zhu, Y. J.; Liu, Y. H.; Wang, C. S. Electrochemical Performance of Porous Carbon/Tin Composite Anodes for Sodium-Ion and Lithium-Ion Batteries. *Adv. Energy Mater.* **2013**, *3*, 128–133.

(31) Liu, Y.; Xu, Y.; Zhu, Y.; Culver, J. N.; Lundgren, C. A.; Xu, K.; Wang, C. S. Tin-Coated Viral Nanoforests as Sodium-Ion Battery Anodes. *ACS Nano* **2013**, *7*, 3627–3634.

(32) Zhu, H.; Jia, Z.; Chen, Y.; Weadock, N.; Wan, J.; Vaaland, O.; Han, X.; Li, T.; Hu, L. Tin Anode for Sodium-Ion Batteries Using Natural Wood Fiber as a Mechanical Buffer and Electrolyte Reservoir. *Nano Lett.* **2013**, *13*, 3093–3100.

(33) Xiao, L. F.; Cao, Y. L.; Xiao, J.; Wang, W.; Kovarik, L.; Nie, Z. M.; Liu, J. High Capacity, Reversible Alloying Reactions in SnSb/C Nanocomposites for Na-Ion Battery Applications. *Chem. Commun.* **2012**, *48*, 3321–3323.

(34) Ji, L. W.; Gu, M.; Shao, Y. Y.; Li, X. L.; Engelhard, M. H.; Arey, B. W.; Wang, W.; Nie, Z. M.; Xiao, J.; Wang, C. M.; Zhang, J. G.; Liu, J. Controlling SEI Formation on SnSb-Porous Carbon Nanofibers for Improved Na Ion Storage. *Adv. Mater.* **2014**, *26*, 2901–2908.

(35) Li, L.; Seng, K. H.; Li, D.; Xia, Y. Y.; Liu, H. K.; Guo, Z. P. SnSb@Carbon Nanocable Anchored on Graphene Sheets for Sodium Ion Batteries. *Nano Res.* **2014**, *7*, 1466–1476.

(36) Qian, J. F.; Xiong, Y.; Cao, Y. L.; Ai, X. P.; Yang, H. X. Synergistic Na-Storage Reactions in Sn<sub>4</sub>P<sub>3</sub> as a High-Capacity, Cycle stable Anode of Na-Ion Batteries. *Nano Lett.* **2014**, *14*, 1865–1869.

(37) Kim, Y.; Kim, Y.; Choi, A.; Woo, S.; Mok, D.; Choi, N. S.; Jung, Y. S.; Ryu, J. H.; Oh, S. M.; Lee, K. T. Tin Phosphide as a Promising Anode Material for Na-Ion Batteries. *Adv. Mater.* **2014**, *26*, 4139–4144.

(38) Li, W. J.; Chou, S. L.; Wang, J. Z.; Kim, J. H.; Liu, H. K.; Dou, S. X. Sn<sub>4+x</sub>P<sub>3</sub>@Amorphous Sn-P Composites as Anodes for Sodium-Ion Batteries with Low Cost, High Capacity, Long Life, and Superior Rate Capability. *Adv. Mater.* **2014**, *26*, 4037–4042.

(39) Zhou, X. S.; Liu, X.; Xu, Y.; Liu, Y. X.; Dai, Z. H.; Bao, J. C. An SbO<sub>x</sub>/Reduced Graphene Oxide Composite as a High-Rate Anode Material for Sodium-Ion Batteries. *J. Phys. Chem. C* **2014**, *118*, 23527–23534.

(40) Su, D. W.; Xie, X. Q.; Wang, G. X. Hierarchical Mesoporous SnO Microspheres as High Capacity Anode Materials for Sodium-Ion Batteries. *Chem. - Eur. J.* **2014**, *20*, 3192–3197.

(41) Wang, C.; Wu, H.; Chen, Z.; McDowell, M. T.; Cui, Y.; Bao, Z. N. Self-Healing Chemistry Enables the Stable Operation of Silicon Microparticle Anodes for High-Energy Lithium-Ion Batteries. *Nat. Chem.* **2013**, *5*, 1042–1048.